

Voltage-Tunable Q Factor in Photonic Crystal Microcavity

A.I. KRASNOV^{1,2,†}, P.S. PANKIN^{1,2,†,*}, D.S. BUZIN^{1,2,†}, G.A. ROMANENKO^{1,3,†}, V.S. SUTORMIN^{1,2}, F.V. ZELENOV^{4,3}, A.N. MASYUGIN^{4,3}, M.N. VOLOCHAEV¹, S.YA. VETROV^{2,1}, AND I.V. TIMOFEEV^{1,2}

¹Kirensky Institute of Physics, Krasnoyarsk Scientific Center, Siberian Branch, Russian Academy of Sciences, Krasnoyarsk, 660036 Russia

²Siberian Federal University, Krasnoyarsk, 660041 Russia

³Siberian State University of Science and Technology, Krasnoyarsk, 660037 Russia

⁴AO NPP Radiosvyaz, Krasnoyarsk, 660021 Russia

[†]These authors equally contributed to this work

*Corresponding author: pavel-s-pankin@iph.krasn.ru

Compiled February 6, 2023

A photonic crystal microcavity with the tunable Q factor has been implemented on the basis of a bound state in the continuum using the advanced liquid crystal cell technology platform. It has been shown that the Q factor of the microcavity changes from 100 to 360 in the voltage range of 0.6 V.

© 2023 Optica Publishing Group

<http://dx.doi.org/10.1364/ao.XX.XXXXXX>

Bound states in the continuum (BICs) are the nonradiative localized eigenmodes implemented in an open system. The BIC was first reported by von Neumann and Wigner in 1929 as a solution of the problem for a quantum particle in the finite oscillating potential [1]. The wave function of a particle is localized, while its energy is positive and lies within a continuum of propagating states. The BIC is a general wave phenomenon, which occurs not only in quantum mechanics, but also in radio physics, photonics, and acoustics [2–6]. Changing the parameters of a system near the BIC, one can control the coupling between a localized mode and the continuum of propagating waves and thereby tune the radiation component of the system Q factor. In practice, due to the finite geometric length of structures, imperfection of fabrication techniques used, and absorption of materials, the amplitude of the Fano resonances with a finite Q factor [7–9] at the BIC points turns to zero. In this case, we can speak about the implementation of quasi-BICs. The BIC concept was used in various photonics applications, in particular, in lasers [10, 11], sensors [12–15], waveguides [16, 17], optical switches [18], nonlinear amplifiers [19], etc. According to the mechanism of implementation, the BICs are divided in several classes [2–6]. The symmetry-protected BICs (SP BICs) are based on opposite symmetries of localized modes and propagating waves, which yields the zero overlap integral [20, 21]. The Friedrich–Wintgen (accidental) BICs (FW BICs) originate from the destructive interference of waves outgoing from a cavity [16, 22].

According to the Lee’s theorem [23], in a 1D multilayer model,

the transmission zeros and, consequently, BICs, cannot be implemented. This theorem, however, is not generalized to the 1D multilayers of anisotropic materials, in which, as in the 2D and 3D models, the BICs were also implemented [24–26]. The authors of [27, 28] demonstrated a trilayer waveguide consisting of birefringent materials, which supports the waveguide quasi-BICs. The rest 1D models that have been proposed to date are based on photonic crystals (PhCs) with an anisotropic defect layer [29–34].

In this study, an optical microcavity model [30] with the voltage-tunable Q factor is implemented on the basis of a BIC. Figure 1(a) shows a microcavity consisting of two identical mirrors formed from 1D PhCs separated by a liquid crystal (LC) resonator layer.

The PhCs were formed on glass substrates pre-coated with aluminum-doped zinc oxide (AZO) with a refractive index (RI) of $n_{\text{AZO}} = 1.8 + i0.062$ [35] (hereinafter, the RIs of all the materials are given for a wavelength of $\lambda = 570$ nm) and a thickness of $d_{\text{AZO}} = 100$ nm. The PhC includes $N = 8$ periods consisting of a silicon nitride (Si_3N_4) layer and a silicon dioxide (SiO_2) layer formed by plasma-enhanced chemical vapor deposition. The RIs and layer thicknesses are $n_{\text{Si}_3\text{N}_4} = 2.15$ [36], $d_{\text{Si}_3\text{N}_4} = 80$ nm and $n_{\text{SiO}_2} = 1.45$ [37], $d_{\text{SiO}_2} = 153$ nm. To obtain the symmetry, the PhC was additionally coated with an unpaired Si_3N_4 layer. Polyvinyl alcohol (PVA) layers with an RI of $n_{\text{PVA}} = 1.48$ [38] and a thickness of $d_{\text{PVA}} = 100$ nm were formed on each PhC by the spin-coating method. The mechanical rubbing of the PVA layers ensured a homogeneous planar alignment of the LC. The PhC mirrors were placed into a metal holder with tuning screws to make a uniform gap, which was determined by teflon spacers with a thickness of about $d = 9.57$ μm . The gap between PhC mirrors was filled by 4-pentyl-4'-cyanobiphenyl (5CB) nematic LC with RIs of $n_{\perp} = \sqrt{\epsilon_{\perp}} = 1.55$ and $n_{\parallel} = \sqrt{\epsilon_{\parallel}} = 1.74$ [39–41] by a capillary method. The preferred alignment of the long axes of LC molecules is described by the unit vector $\mathbf{a} = [\cos(\phi) \cos(\theta), \sin(\phi) \cos(\theta), \sin(\theta)]$, which is called the director [42]. In nematic LC the director coincides with the orientation of optical axis (OA) determined, according to Fig. 1(a), as a direction of the major semiaxis of the

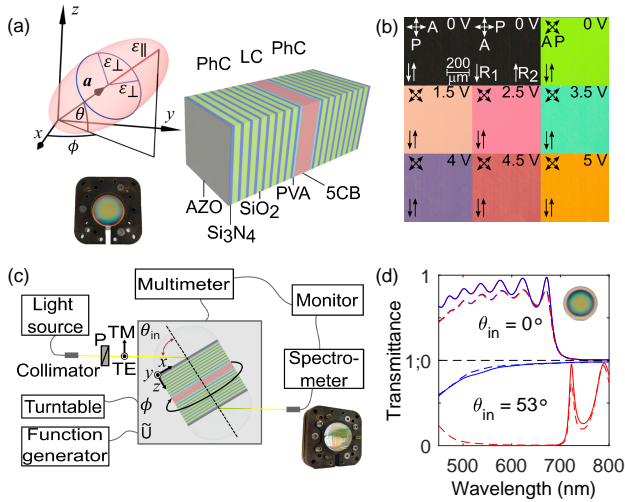


Fig. 1. (a) PhC microcavity model. The inset shows the orientation of an LC permittivity ellipsoid. The microcavity is presented in the photograph. (b) Polarizing optical microscope images of the LC layer texture taken in crossed polarizers at different applied voltages. R_1 and R_2 are the PVA rubbing directions. Crossed double arrows show the direction of the polarizer (P) and analyzer (A). (c) Scheme for measuring the microcavity transmittance spectra. The TE and TM vectors show the direction of the electric field at the corresponding polarizations. The photograph in the inset shows the microcavity with hemispherical lenses. (d) Measured (dashed line) and calculated (solid line) PhC transmittance spectra for the TE (red) and TM (blue) waves. The top and bottom plots correspond to the normal incidence of light and the incidence at the Brewster's angle, respectively. The photograph of the PhC is shown in the inset.

71 permittivity ellipsoid.

72 Figure 1(b) presents polarizing microscopy images of the
 73 optical texture of the LC layer. When the rubbing direction
 74 is parallel to the polarizer or analyzer, a uniform dark texture
 75 can be seen. The maximum intensity of the transmitted light
 76 is observed upon rotation of the crossed polarizers by 45° (the
 77 top row in Fig. 1(b)). These optical textures confirm the planar
 78 LC alignment. The conducting transparent AZO layers make
 79 it possible to apply 1 kHz AC voltage to the LC layer to avoid
 80 blocking of the external field by ions in the LC. It can be seen in
 81 Fig. 1(b) (the middle and bottom rows) that the applied voltage
 82 changes the color of the optical texture of the LC layer, which is
 83 evidence of the change in the LC orientational structure.

84 Figure 1(c) presents a scheme for measuring the microcavity
 85 transmittance spectra. The incoherent radiation of a halo-
 86 gen lamp from a Thorlabs OSL2 source propagates through
 87 an optical fiber and focuses with a collimator in a spot about
 88 2 mm in diameter. After the transmittance through a polarizer,
 89 the TE-polarized (TE wave) or TM-polarized (TM wave)
 90 radiation passes into the microcavity through hemispherical
 91 glass lenses with an RI of $n_G = 1.5$. The lenses are glued
 92 to the glass substrates of the microcavity using immersion
 93 oil with an RI of $n_{oil} = 1.5$ to eliminate an air gap. In-
 94 troducing the radiation through the glass lenses at an angle
 95 of $\theta_{in} = \arcsin[(n_{Si_3N_4}/n_G) \sin(\arctan(n_{SiO_2}/n_{Si_3N_4}))] \approx 53^\circ$,
 96 one can implement the Brewster effect for the TM wave at
 97 the Si_3N_4/SiO_2 interfaces [43]. The outgoing radiation is col-

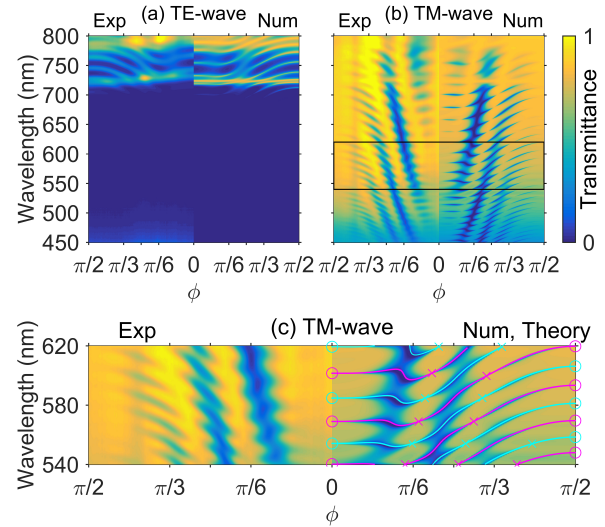


Fig. 2. Transmittance spectra of the optical microcavity at different azimuthal angles ϕ of the LC OA for (a) TE and (b, c) TM waves. The left-hand panels show the measured spectra and the right-hand panels present the calculated ones. The black rectangle in (b) is zoomed in (c). Solid lines in (c) correspond to the solutions of the problem on the eigenvalues of an open cavity for the even (magenta lines) and odd (cyan lines) modes. The solutions are shown by circles for the SP BIC problem and by crosses for FW BIC problem.

98 lected in a fiber optic collimator connected to an OCEAN FX-UV-
 99 VIS spectrometer. The microcavity is mounted on an Thorlabs
 100 KPRM1E/M motorized precision rotation stage, which makes it
 101 possible to change the azimuthal angle ϕ of the LC OA orienta-
 102 tion. The external voltage applied to LC layer using an Aktakom
 103 AWG-4150 function generator can change the polar angle θ of
 104 the LC OA orientation. The value and frequency of the applied
 105 voltage are controlled with an Aktakom ABM-4552 multimeter.
 106 The operation of all the units and recording of the spectra are
 107 monitored using a personal computer.

108 Figure 1(d) presents the PhC transmittance spectra measured
 109 and calculated by the Berreman transfer matrix method [44].
 110 It can be seen that, under normal incidence of light, there is a
 111 photonic band gap (PBG) with the center at $\lambda_{PBG} = 800$ nm for
 112 both the TE and TM waves. When the light falls at the Brewster's
 113 angle, the PBG shifts to the visible range and $\lambda_{PBG} = 570$ nm
 114 for the TE wave. The PBG for the TM wave vanishes due to the
 115 Brewster effect. Thus, in a certain wavelength range, the PhC
 116 is nontransparent for the TE waves and transparent for the TM
 117 ones.

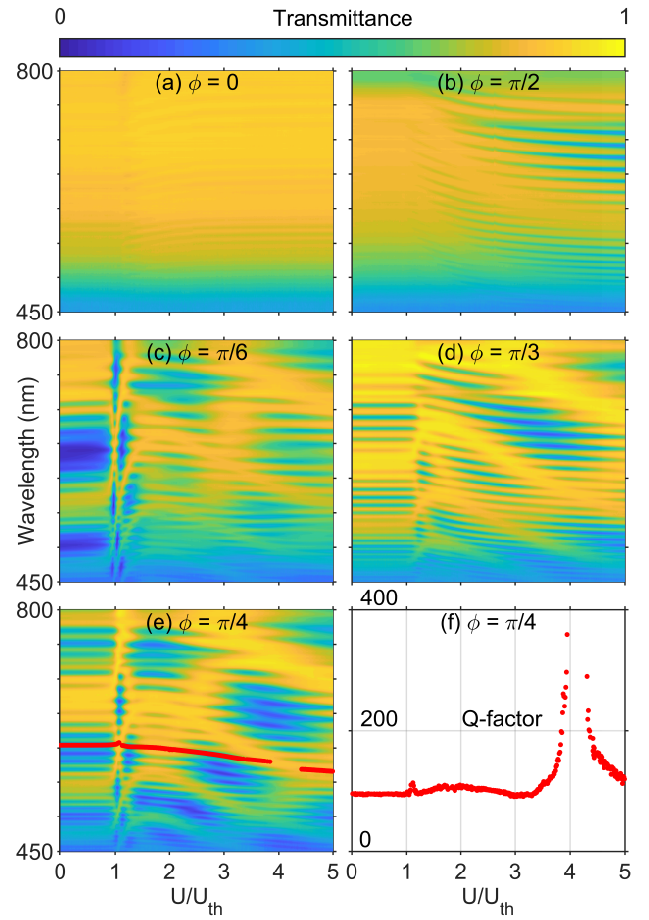
118 Figure 2 illustrates the transformation of the transmittance
 119 spectra of the microcavity filled with the LC upon variation in
 120 the azimuthal angle ϕ of the LC OA orientation. Figure 2(a)
 121 shows that the spectrum does not change in the PBG region for
 122 the TE waves, which demonstrates the absence of resonances.
 123 On the other hand, the spectrum for the TM waves contains
 124 numerous resonant lines in the same spectral range (see Fig. 2(b)).
 125 The rotation of the LC OA causes the change in the position and
 126 width of the resonant lines. It is consequence of the changes
 127 both in the optical width of the LC layer and in the coupling
 128 between the localized modes and the waves propagating in the
 129 PhC waveguides.

130 The behavior of the spectra can be qualitatively explained
 131 by dividing the total electric field strength E of light in the LC
 132 into contributions of the ordinary wave (o wave) E_o and ex-
 133 traordinary wave (e wave) E_e : $E = E_e + E_o$. The polariza-
 134 tion directions of the o and e waves are given by the vectors
 135 $E_o = E_o [a \times \kappa_o]$ and $E_e = E_e \left[a - \frac{\epsilon_e(\alpha)}{\epsilon_o} \kappa_e(\kappa_e a) \right]$ [45], respec-
 136 tively. Here, $\kappa_{o,e} = [\kappa_{o,ex}; 0; \kappa_{o,eZ}]$ is the unit vector along the
 137 direction of propagation of the o, e wave; $\epsilon_o = \epsilon_{\perp}$ is the per-
 138 mittivity for the o wave, and $\epsilon_e(\alpha)$ is the permittivity for the e
 139 wave, which has the values $\epsilon_{\perp} \leq \epsilon_e(\alpha) \leq \epsilon_{\parallel}$ and is determined
 140 by the angle α between the vectors a and κ_e . Since the o and e
 141 waves have different permittivities, they have different phase
 142 incursions during propagation through the LC layer. In the general
 143 case, for the angles $\phi \neq 0$ and $\theta \neq 0$, all the components of
 144 the o and e waves are nonzero: $E_{o,e} = [E_{o,ex}, E_{o,ey}, E_{o,eZ}]$; i.e.,
 145 the TE and TM waves are mixed in the LC layer.

146 The measured and calculated spectra in Fig. 2(b) show that
 147 the resonant lines collapse at $\phi = 0$ and $\phi = \pi/2$. The positions
 148 of the collapses coincide with the solutions of the problem on
 149 the SP BICs [30], which are shown by circles in Fig. 2(c). At
 150 $\theta = 0$ and $\phi = 0$, the o wave has a projection only on the TE
 151 wave: $E_o = [0, E_{oy}, 0]$ and the e wave has a projection only on
 152 the TM wave: $E_e = [E_{ex}, 0, E_{ez}]$ (see Figs. 1(a,b)). At $\theta = 0$ and
 153 $\phi = \pi/2$, the situation is opposite: $E_o = [E_{ox}, 0, E_{oz}]$, $E_e =$
 154 $[0, E_{ey}, 0]$. This means that, in these cases, the propagating TM
 155 wave is not converted into the TE wave, which can be localized
 156 due to the PBG. This explains qualitatively also the red shift of
 157 the resonant lines in Fig. 2(b) with increasing angle ϕ . For the
 158 localized TE waves with the only y component, the RI changes
 159 from the minimum value $n|_{\phi=0}^{\theta=0} = n_{\perp}$ to the maximum one
 160 $n|_{\phi=\pi/2}^{\theta=0} = n_{\parallel}$. The behavior of the resonant lines is confirmed
 161 also by the numerical calculation and solution of the problem
 162 on the eigenvalues of an open system [30]. Figure 2(c) shows the
 163 spectral position of the resonances $\lambda_0 = 2\pi/\omega_0$ obtained from
 164 the eigenvalue $\omega_r = \omega_0 - i\gamma$.

165 The collapses of the resonant lines can be observed also at the
 166 intermediate angles $\phi \neq 0, \pi/2$. The positions of the collapses
 167 coincide with the solutions of the problem on the FW BICs [30]
 168 shown by crosses in Fig. 2(c). When the total projection of the
 169 contributions of the o and e waves on the TM wave at the output
 170 of LC layer is zero $E_x = E_{ex} + E_{ox} = 0$, the energy cannot be
 171 brought out of the cavity by the propagating TM waves. This
 172 differs the SP BICs from the FW BICs, in which not only the
 173 TE component of the total field is localized in the LC layer due
 174 to the PBG, but also the TM component, due to the destructive
 175 interference of the waves at the output of the LC layer [30]. As
 176 it was shown in [30, 34], the LC layer in this case plays the role
 177 of a full-wave phase plate, which recovers the state of polariza-
 178 tion at the output identical to that at the input [46]. In both
 179 cases, when the SP BICs or FW BICs are implemented, there
 180 is no coupling between the localized and propagating waves,
 181 which makes zero radiation component of the imaginary part
 182 of the eigenvalue $\gamma_{rad} = 0$; $\gamma = \gamma_{rad} + \gamma_{ext}$. In the spectrum it
 183 appears as a vanishing amplitude of the resonant line, the width
 184 of which at the quasi-BIC point is only determined by the nonra-
 185 diative extinction loss, including the absorption and scattering
 186 $\Delta\omega = 2\gamma_{ext}$. Between the two angles ϕ corresponding to the BIC
 187 implementation, the radiation component of the resonant line
 188 width γ_{rad} changes from zero to the finite value and vice versa.
 189 It allows to consider this situation as the implementation of the
 190 resonances with the tunable quality factor $Q = \omega_0/2\gamma$.

191 Figure 3 illustrates the transformation of the transmittance



192 **Fig. 3.** (a–e) Measured transmittance spectra of the optical mi-
 193 crocavity at different values of applied voltages U ; $U_{th} \approx 1.2 V$
 194 is the threshold voltage for LC reorientation. (f) Q factor of the
 195 resonant line (red dots in (e)) calculated from the FWHM.

192 spectra of the microcavity upon variation in the voltage applied
 193 to the LC layer at constant azimuthal angles ϕ of the LC OA
 194 orientation. It can be seen from the spectra that, at the voltages
 195 below the threshold value of the Fredericks effect [42] $U < U_{th}$,
 196 the positions and widths of the resonant lines do not change.
 197 The voltage $U = U_{th}$ corresponds to the beginning of the LC
 198 reorientation. With a further increase in the voltage $U \geq U_{th}$,
 199 the director rotates toward the external electric field direction
 200 (along the z axis); i.e., the polar angle θ increases (see Fig. 1(a)).
 201 At $\phi = 0$, for any polar angle θ , the o wave has a projection
 202 only on the TE wave, while the e wave has a projection only on
 203 the TM wave. The propagating TM wave is not converted
 204 to the TE wave at any applied voltage U . Therefore, the weak
 205 resonances in Fig. 3(a), which have fixed widths, correspond
 206 to the localized TM waves. They arise due to the low reflectance
 207 at the interface between the PVA layer and the first Si_3N_4 layer.
 208 These resonances, as a background of the resonances with the
 209 tunable Q factor, can also be seen in Fig. 3(b) up to the thresh-
 210 old voltage, as well as in Figs. 2(b,c) at $\phi = 0, \pi/2$. Intermixing
 211 of the TE and TM waves in the LC layer in the general case
 212 of $\phi \neq 0$ and $\theta \neq 0$ leads to the occurrence of the resonances
 213 with the tunable Q factor, as can be seen in Figs. 3(b–e). At
 214 certain voltages U , one can see the collapses of the resonant
 215 lines corresponding to the FW BICs (the mechanism of their

implementation was explained above). At an external voltage of $U > 5U_{th}$, the resonant lines in the spectrum remain almost invariable. This is due to the fact that, at high voltages, the LC director, except for the thin surface layer, aligns along the applied field direction [42]. This explains also the blue shift of the resonant lines, since, in the limit case of high voltages, the angle is $\theta = \pi/2$ and for the localized TE wave, which has only the y component the LC RI is equal to the minimum value $n_{\phi}^{\theta=\pi/2} = n_{\perp}$ (Fig. 1(a)). In Fig. 3(f), the Q factor is presented for one of the resonant lines from Fig. 3(e). It can be seen that the Q factor sharply increases upon approaching the FW BIC in the vicinity of $U \approx 4.1U_{th}$. The measured Q factor changes from 100 to 360 in the voltage range from $3.4U_{th}$ to $3.9U_{th}$, i.e., by $0.5U_{th} = 0.6$ V. The sensitivity of the Q factor to the change in the applied voltage is $\Delta Q/\Delta U = 433$ V⁻¹.

Thus, a photonic crystal microcavity with a liquid crystal defect layer was created, where on the basis of the concept of the bound state in the continuum, we first demonstrated the efficient voltage control by both the position [47–51] and width of the resonant lines. The proposed model can be used for design of energy-efficient photonic devices with the voltage-tunable Q factor.

Acknowledgments. We acknowledge discussions with Dmitrii N. Maksimov. This study was supported by the Russian Science Foundation, project no. 22-22-00687.

Disclosures. The authors declare no conflicts of interest.

Data Availability Statement. The data that support the findings of this study are available from the corresponding author, P.S.P., upon reasonable request.

REFERENCES

1. J. von Neumann and E. P. Wigner, *Phys. Zeitschrift* **30**, 467 (1929).
2. C. W. Hsu, B. Zhen, A. D. Stone, J. D. Joannopoulos, and M. Soljačić, *Nat. Rev. Mater.* **1**, 16048 (2016).
3. A. F. Sadreev, *Reports on Prog. Phys.* (2021).
4. K. L. Koshelev, Z. F. Sadrieva, A. A. Shcherbakov, Y. Kivshar, and A. A. Bogdanov, *Physics-Uspexhi* (2021).
5. S. I. Azzam and A. V. Kildishev, *Adv. Opt. Mater.* **9**, 2001469 (2021).
6. S. Joseph, S. Pandey, S. Sarkar, and J. Joseph, *Nanophotonics* **10**, 4175 (2021).
7. M. F. Limonov, M. V. Rybin, A. N. Poddubny, and Y. S. Kivshar, *Nat. Photonics* **11**, 543 (2017).
8. M. V. Rybin, K. L. Koshelev, Z. F. Sadrieva, K. B. Samusev, A. A. Bogdanov, M. F. Limonov, and Y. S. Kivshar, *Phys. Rev. Lett.* **119**, 243901 (2017).
9. Z. Zhao, C. Guo, and S. Fan, *Phys. Rev. A* **99**, 33839 (2019).
10. A. Kodigala, T. Lepetit, Q. Gu, B. Bahari, Y. Fainman, and B. Kanté, *Nature* **541**, 196 (2017).
11. C. Huang, C. Zhang, S. Xiao, Y. Wang, Y. Fan, Y. Liu, N. Zhang, G. Qu, H. Ji, J. Han, L. Ge, Y. Kivshar, and Q. Song, *Science* **367**, 1018 (2020).
12. A. M. Chernyak, M. G. Barsukova, A. S. Shorokhov, A. I. Musorin, and A. A. Fedyanin, *JETP Lett.* **111**, 46 (2020).
13. I. Yusupov, D. Filonov, A. Bogdanov, P. Ginzburg, M. V. Rybin, and A. Slobozhanyuk, *Appl. Phys. Lett.* **119**, 193504 (2021).
14. C. Schiattarella, G. Sanità, B. G. Alulema, V. Lanzio, S. Cabrini, A. Lamberti, I. Rendina, V. Mocella, G. Zito, and S. Romano, *Biosens. Bioelectron. X* p. 100262 (2022).
15. A. Sadreev, E. Bulgakov, A. Pilipchuk, A. Miroshnichenko, and L. Huang, *Phys. Rev. B* **106**, 085404 (2022).
16. C. W. Hsu, B. Zhen, J. Lee, S. L. Chua, S. G. Johnson, J. D. Joannopoulos, and M. Soljačić, *Nature* **499**, 188 (2013).
17. E. A. Bezus, D. A. Bykov, and L. L. Doskolovich, *Photonics Res.* **6**, 1084 (2018).
18. D. N. Maksimov, A. S. Kostyukov, A. E. Ershov, M. S. Molochev, E. N. Bulgakov, and V. S. Gerasimov, *arXiv Prepr.* (2022).
19. K. Koshelev, S. Kruk, E. Melik-Gaykazyan, J.-H. Choi, A. Bogdanov, H.-G. Park, and Y. Kivshar, *Science* **367**, 288 (2020).
20. E. N. Bulgakov and A. F. Sadreev, *Phys. Rev. B* **78**, 75105 (2008).
21. D. C. Marinica, A. G. Borisov, and S. V. Shabanov, *Phys. Rev. Lett.* **100**, 183902 (2008).
22. H. Friedrich and D. Wintgen, *Phys. Rev. A* **32**, 3231 (1985).
23. H. W. Lee, *Phys. Rev. Lett.* **82**, 2358 (1999).
24. F. Razzaz and M. A. S. Alkanhal, *IEEE Photonics J.* **10**, 1 (2017).
25. I. Quotane, E. H. El Boudouti, and B. Djafari-Rouhani, *Phys. Rev. B* **97**, 24304 (2018).
26. S. Mizuno, *Appl. Phys. Express* **12**, 35504 (2019).
27. J. Gomis-Bresco, D. Artigas, and L. Torner, *Nat. Photonics* **11**, 232 (2017).
28. S. Mukherjee, J. Gomis-Bresco, D. Artigas, and L. Torner, *Opt. Lett.* **46**, 2545 (2021).
29. I. V. Timofeev, D. N. Maksimov, and A. F. Sadreev, *Phys. Rev. B* **97**, 24306 (2018).
30. P. S. Pankin, B.-R. Wu, J.-H. Yang, K.-P. Chen, I. V. Timofeev, and A. F. Sadreev, *Commun. Phys.* **3**, 91 (2020).
31. P. S. Pankin, D. N. Maksimov, K. P. Chen, and I. V. Timofeev, *Sci. Reports* **10**, 13691 (2020).
32. D. O. Ignatyeva and V. I. Belotelov, *Opt. Lett.* **45**, 6422 (2020).
33. J. Yang, Z. Huang, D. N. Maksimov, P. S. Pankin, I. V. Timofeev, K. Hong, H. Li, J. Chen, C. Hsu, Y. Liu, T. Lu, T. Lin, C. Yang, and K. Chen, *Laser Photonics Rev.* **15**, 2100118 (2021).
34. P. S. Pankin, D. N. Maksimov, and I. V. Timofeev, *J. Opt. Soc. Am. B* **39**, 968 (2022).
35. I. A. Tambasov, M. N. Volochaev, A. S. Voronin, N. P. Evsevskaya, A. N. Masyugin, A. S. Aleksandrovskii, T. E. Smolyarova, I. V. Nemtsev, S. A. Lyashchenko, G. N. Bondarenko, and Others, *Phys. Solid State* **61**, 1904 (2019).
36. K. Luke, Y. Okawachi, M. R. E. Lamont, A. L. Gaeta, and M. Lipson, *Opt. letters* **40**, 4823 (2015).
37. L. Gao, F. Lemarchand, and M. Lequime, *J. Eur. Opt. Soc. publications* **8** (2013).
38. M. J. Schnepf, M. Mayer, C. Kuttner, M. Tebbe, D. Wolf, M. Dulle, T. Altantzis, P. Formanek, S. Förster, S. Bals, T. A. F. König, and A. Fery, *Nanoscale* **9**, 9376 (2017).
39. J. Li, C. H. Wen, S. Gauza, R. Lu, and S. T. Wu, *J. Disp. Technol.* **1**, 51 (2005).
40. V. Tkachenko, G. Abbate, A. Marino, F. Vita, M. Giocondo, A. Mazzulla, F. Ciuchi, and L. D. Stefano, *Mol. Cryst. Liq. Cryst.* **454**, 263 (2006).
41. M. S. Sefton, A. R. Bowdler, and H. J. Coles, *Mol. Cryst. Liq. Cryst.* **129**, 1 (1985).
42. L. M. Blinov, *Structure and Properties of Liquid Crystals*, Topics in applied physics (Springer, 2010).
43. S. A. Akhmanov and S. Y. Nikitin, *Physical Optics* (Clarendon Press, 1997).
44. D. W. Berreman, *J. Opt. Soc. Am.* **62**, 502 (1972).
45. F. V. Ignatovich and V. K. Ignatovich, *Uspekhi Fiz. Nauk* **182**, 759 (2012).
46. B. E. A. Saleh and M. C. Teich, *Fundamentals of Photonics*, Wiley Series in Pure and Applied Optics (Wiley, 2007).
47. S. Y. Vetrov and A. V. Shabanov, *J. Exp. Theor. Phys.* **93**, 977 (2001).
48. R. Ozaki, T. Matsui, M. Ozaki, and K. Yoshino, *Jpn. J. Appl. Phys.* **41**, L1482 (2002).
49. R. Ozaki, T. Matsui, M. Ozaki, and K. Yoshino, *Appl. Phys. Lett.* **82**, 3593 (2003).
50. V. G. Arkhipkin, V. A. Gunyakov, S. A. Myslivets, V. Y. Zyryanov, V. F. Shabanov, and W. Lee, *J. Exp. Theor. Phys.* **112**, 577 (2011).
51. P. S. Pankin, V. S. Sutormin, V. A. Gunyakov, F. V. Zelenov, I. A. Tambasov, A. N. Masyugin, M. N. Volochaev, F. A. Baron, K. P. Chen, V. Y. Zyryanov, S. Y. Vetrov, and I. V. Timofeev, *Appl. Phys. Lett.* **119**, 161107 (2021).